

# Lead based halide perovskite surface analysis using DFT and MD

3MQ110 Advanced Materials Modelling using Multiscale Methods

## Abstract

### Authors:

Y.L. de Jong (1250663)  
T.G. de Gijzel (1234126)  
T.A. van de Laar (1223368)

### Supervisors:

M.C.W.M. Pols  
S. Apergi  
S.X. Tao

*In recent years, we have seen a lot of breakthroughs in the development of perovskite semiconductors. The fully inorganic  $\text{CsPbI}_3$  can be created at an industrial scale and has high photovoltaic conversion efficiency. One of the main problems however is the stability of both the bulk and surface of this material. The stability of both these types is investigated using MD and DFT. Here it is shown that the orthorhombic  $\gamma$  phase is most stable in the bulk and slab configurations. The most stable surface is determined to be the CsI surface. Furthermore, it is shown that defects in the lattice that arise during the fabrication may lead to instabilities in the bulk material. The lattice parameters are obtained using both DFT and MD and the values for bulk structures are in good agreement with literature. The values for slabs are compared between the methods and show a small discrepancy between them. Lastly, we use DFT for band structure calculations and report band gaps for  $\alpha$ -,  $\beta$ - and  $\gamma$ - $\text{CsPbI}_3$  in bulk and slab structures.*

Date: April 11, 2022

## 1 Introduction

The energy demand is growing every year, and the current climate change crisis requires the development of new renewable energy sources to provide the needed energy. Solar photovoltaics (PV) and wind energy are expected to account for about two-thirds of the renewable energy growth.<sup>1</sup> Currently, silicon-based solar cells are dominating the photovoltaic market.<sup>2</sup> These solar cells have benefited from reduced costs due to the advancements in the field, but the indirect band gap of silicon makes the photovoltaic cell inefficient and the high-temperature processing gives a fundamental finan-

cial barrier. Alternatives to silicon are welcome, one of which is the organic-inorganic halide perovskites.

The term “perovskite” describes a class of materials, which follow the following formula:  $\text{AMX}_3$ , where the A atom describes an organic or inorganic cation, the M atom describes the metal cation and the X atom is a halide anion. Different halide anions, metal cations and A cations can all work well in optoelectronic perovskite devices, but one should carefully look at the properties of the combinations of the atoms in the design of a perovskite solar cell (PCS). The two most studied perovskites are two organic materials:  $\text{CH}_3\text{NH}_3\text{PbI}_3$  or

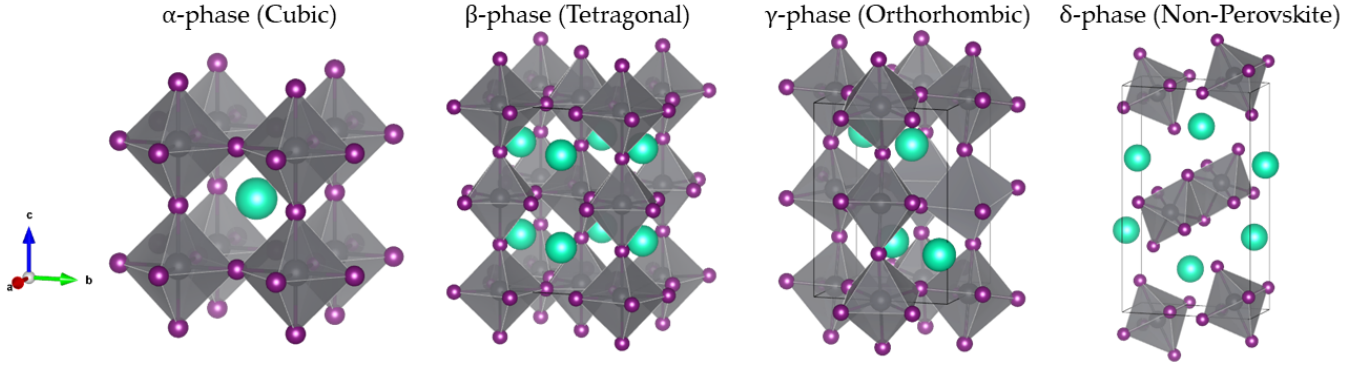


Figure 1: A schematic representation of the different structural phases of  $\text{CsPbI}_3$ .

$\text{MAPbI}_3$  and  $\text{NH}_2\text{CHNH}_2\text{PbI}_3$  or  $\text{FAPbI}_3$ .<sup>3</sup> The materials exhibit suitable electronic properties for devices, such as long-range electron and hole diffusion lengths, high carrier mobilities and an appropriate band gap.<sup>4</sup> Even though these materials have been studied intensively in the past couple of years, the organic-inorganic hybrid perovskites suffer from degradation of the organic component, resulting in thermal instabilities. One alternative to the inorganic-organic hybrid perovskite is to substitute Cs in for the A atom. In cubic structures, the ionic radii of the atoms in the  $\text{AMX}_3$  perovskite should fulfill a condition to maintain high-symmetry structure, specifically that the tolerance factor  $t = (R_A + R_X)/(\sqrt{2}(R_M + R_X))$  should be approximately 1, where  $R_A$ ,  $R_M$  and  $R_X$  are the radii of the A, M and X atom respectively. This means that the A atom should be large so that the cubic structure is not distorted, but the A atom should also have one valence electron. Cs is almost the largest element in Group I, so Cs is a suitable element. Still, Cs is too small to fulfill the structural requirement, so  $\text{CsPbI}_3$  suffers from structural instabilities.<sup>5</sup> Typical metal cations for PCSs are Pb and Sn.  $\text{CsSnI}_3$  based solar cells have a small bandgap, around 1.3 eV, which might be ideal for a PCS.<sup>6</sup> However,  $\text{Sn}^{2+}$  is chemically unstable and oxidizes to the tetravalent  $\text{Sn}^{4+}$ , resulting in Sn vacancies and a low performance of the PSC. Pb based PCSs are chemically more stable but suffer from a higher bandgap and a toxic component.

Here, we study Pb based perovskite materials, which can be produced at an industrial scale,<sup>7</sup> and to obtain a bandgap that is as close to the ideal bandgap from the Shockley-Queisser limit,<sup>8</sup> we study I based perovskites instead of Br and Cl. We provide an analysis of  $\text{CsPbI}_3$  focusing on structural and electronic properties of the black  $\text{CsPbI}_3$ , so the  $\alpha$ -,  $\beta$ - and  $\gamma$ -phase, and yellow  $\text{CsPbI}_3$  or  $\delta$ -phase, see Fig. 1. Next to a study

of bulk properties, we analyze surface features. Due to the interruption of the periodicity, states are generated that are surface-specific deviating from the states in bulk. These states can affect the performance of devices, hence understanding the surface properties of the metal halide perovskite can help the improvement of efficiency and stability in general.<sup>9</sup>

## 2 Methods

### 2.1 Molecular Dynamics

All MD simulations are done using the Amsterdam Modeling Suite<sup>10</sup> using a ReaxFF<sup>11–13</sup> (reactive force field) generated from DFT simulations.<sup>14</sup> All simulations start with a structure which was taken from the materials project database.<sup>15</sup> The equilibrium geometries of the materials are obtained through geometry optimizations. From this optimized geometry, the lattice parameters can be obtained. These can afterwards be compared to the values obtained by a DFT simulation. The actual MD simulation is run for 1 ns with a step size of 0.25 fs. A Berendsen Thermostat<sup>16</sup> with a damping constant of 100 fs and a Berendsen Barostat with a damping constant of 2500 fs are used to create a NPT ensemble. The torsions are set to 2013. A force-field compatible with the bulk phase of  $\text{CsPbI}_3$  was used.<sup>14</sup> For bulk simulations, a lattice with a size of approximately  $(5 \times 5 \times 5)$  is used. For slab simulations, a slab with approximately 5 layers and cut at the (001) miller indices. The results are checked for relaxation using the energy of the system over time, if the energy of the system stays constant for over 1 ns the system is considered stable. Another method of checking the stability of the system can be done by a visual inspection of the lattice for defects. The lattice parameters are obtained from the relaxed systems at 0 K (i.e. no initial

thermal velocity). These constants are measured using the VESTA tool.<sup>17</sup>

## 2.2 Density Functional Theory

We use density functional theory (DFT) calculations to obtain the equilibrium structures of each phase and the corresponding formation energies and band structures. All DFT calculations are performed using the Vienna Ab-Initio Simulation Package (VASP), where the projector augmented wave (PAW) method is implemented.<sup>18–23</sup> To obtain the electronic-correlation energy the Perdew, Burke and Ernzerhof (PBE) functional is used within the generalized gradient approximation (GGA). For the electronic optimization, an energy convergence criterion of  $10^{-5}$  eV is used, and for ionic relaxation, we use a force convergence criterion of  $2 \times 10^{-2}$  eV/Å. The calculations are performed using a  $(4 \times 4 \times 4)$ ,  $(3 \times 3 \times 4)$ ,  $(3 \times 3 \times 3)$ , and  $(6 \times 3 \times 2)$  Monkhorst-Pack  $k$ -point scheme for the  $\alpha$ -,  $\beta$ -,  $\gamma$ - and  $\delta$ -CsPbI<sub>3</sub> in the bulk respectively. Similar to the MD simulations, slabs are used where the termination in the periodic structure is in the (001) direction. The CsI-terminated slabs consist of 3 layers of PbI<sub>2</sub> and 4 layers of CsI, and the PbI<sub>2</sub> terminated slabs consists of 4 layers of PbI<sub>2</sub> and 3 layers of CsI. For the slabs, different Monkhorst-Pack  $k$ -point schemes are used, specifically  $(4 \times 4 \times 1)$  for the  $\alpha$ -,  $\beta$ -, and  $\gamma$ -phases. Furthermore, we use an energy cut-off of 500 eV and a Gaussian smearing for the occupied and unoccupied states.

Before any information about the structures can be extracted, the structures have to be relaxed. The cubic



(a) Cubic bulk structure with 4 randomly placed vacancies. (b) Cubic slab structure with 4 randomly placed vacancies. The top interface is simulated with MD at 700 K after 0.3 ns. In the red area a destabilising PbI cluster can be seen forming. The bottom interface is simulated with MD at 700 K after 0.15 ns. The top shows degradation into PbI structures.

Figure 2: Degradation of unstable cubic structures

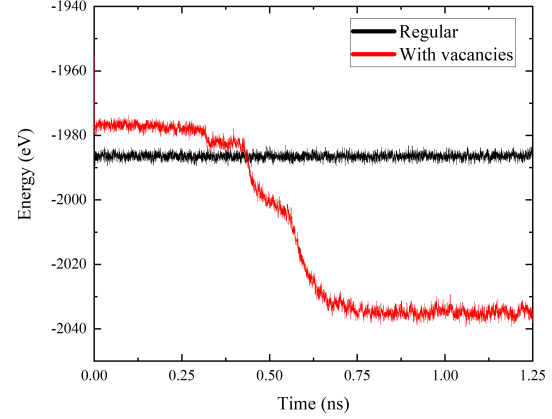


Figure 3: Energy of a cubic lattice with defects at 700 K

structure in bulk is relaxed by allowing to change the positions of the ions in the ionic steps in the first iteration, and by allowing to change the cell volume in the ionic steps in the second iteration. This process is repeated until an equilibrium structure is reached, and is needed due to the soft nature of the lattice. For the relaxation of the tetragonal, orthorhombic  $\gamma$  and orthorhombic  $\delta$  structure in bulk, we allow both the positions of the ions and the cell volume to change, and also the cell shape. For slab structures, only the positions of the ions are relaxed in the ionic steps, and a dipole correction was implemented to account for the errors in the potential and the forces introduced by the periodic boundary conditions. The equilibrium structures can be analyzed using the VESTA tool<sup>17</sup> and can be used as an input structure file for the band structure calculations. For the band structure calculation, we perform a self-consistent calculation with a  $k$ -point grid spanning the entire Brillouin zone which gives a charge density of the structure. The charge density is then used to obtain the eigenvalues and the density of states (DOS).

## 3 Results

### 3.1 Stability

The different phases of CsPbI<sub>3</sub> are subject to structural instabilities. We investigate the nature of these instabilities and the differences and similarities between bulk and surface material. To this end, we consider the formation energy of each phase, to give a relative indication of the stability of each phase, and common structural defects are identified.

### 3.1.1 Bulk stability

The formation energy of each phase in bulk is calculated with:<sup>24</sup>

$$E_{f,i} = E_i - E_{\text{PbI}_2} - E_{\text{CsI}}, \quad (1)$$

where  $i$  indicates one of the phases, and each energy is computed for a single  $\text{CsPbI}_3$ ,  $\text{PbI}_2$ , or  $\text{CsI}$  molecule w.r.t. an arbitrary reference. Table 1 shows the formation energy for each of the four phases. It can be seen that, from the  $\alpha$ - toward the  $\delta$ -phase, the configuration becomes progressively more stable, which is in line with former research.<sup>24</sup>

One source of defects in the  $\text{CsPbI}_3$  lattice is the formation, diffusion and clustering of I vacancies. These vacancies originate during the growth of the crystal lattice itself.<sup>25,26</sup> MD-simulations of the bulk with induced iodine vacancies show the growth of  $\text{PbI}$  clusters inside of the lattice, degrading the stability of the system. These formations are highlighted in Fig. 2a. A regular cubic lattice without any defects is simulated for 1.25 ns at 700 K. The simulation showed that the system was stable for at least the entire simulation run. A graph representing the energy of the system can be seen in Fig. 3. It is shown that a clear equilibrium has been reached as the energy of the system is stable at a nearly constant value.

When defects, in this case, 4 randomly placed iodine vacancies, are introduced in the lattice, a clear change in the behaviour is seen. The energy of the system is not steady at a constant value. It decreases to a lower energy configuration, and therefore, to a more favourable state, which is depicted in Fig. 3. At around 0.3 ns the structure starts to degrade, and the aforementioned lead iodine clusters start to form. The  $\text{PbI}_2$  structures distort the lattice and eventually destroy any sense of structure.

Table 1: The formation energy of  $\alpha$ -,  $\beta$ -, and  $\gamma$ - $\text{CsPbI}_3$ . Slab<sub>1</sub> and slab<sub>2</sub> correspond to slabs with  $\text{PbI}_2$ -, and  $\text{CsI}$ -layers on the outside, respectively. Note that the found formation energies of the bulk material and the two kinds of slabs are mutually incomparable, and are a mere measure for the *relative* stability of each configuration w.r.t. the other configurations of the same kind (bulk, slab<sub>1</sub>, or slab<sub>2</sub>).

	$E_\alpha$ (eV)	$E_\beta$ (eV)	$E_\gamma$ (eV)	$E_\delta$ (eV)
Bulk	-0.046	-0.096	-0.110	-0.140
Slab <sub>1</sub>	0.528	0.881	1.148	-
Slab <sub>2</sub>	0.018	-0.032	-0.339	-

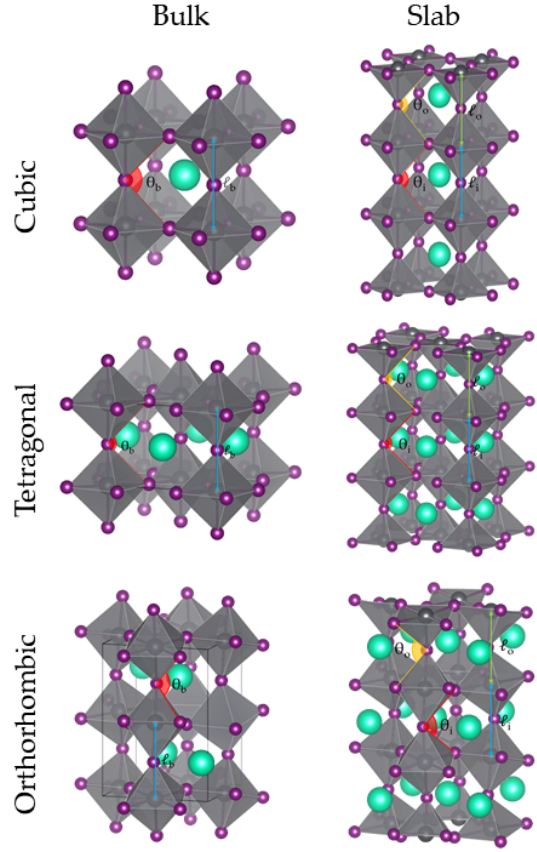


Figure 4: An overview of the relaxed configurations of  $\alpha$ -,  $\beta$ - and  $\gamma$ - $\text{CsPbI}_3$ , for both the bulk and the  $\text{PbI}_2$ -terminated slab. For the slabs, the bonds and angles of the middle layer and the top layer are indicated. The outer slab indicates the top or bottom layer in the slab, the values are the same, and the inner layer indicates the middle layer.

### 3.1.2 Slab stability

To investigate the stability of a  $\text{CsPbI}_3$ -surface specifically, we consider differences in formation energy between slabs of the  $\alpha$ ,  $\beta$ , and  $\gamma$  phases. As mentioned before, all slabs are terminated at the (001) Miller indices and are terminated after a  $\text{PbI}_2$ -layer or a  $\text{CsI}$ -layer. The formation energies of the surface configurations are calculated with:

$$E_{f,i} = E_{\text{CsPbI}_3,i} - n_{\text{Cs},i} E_{\text{CsI}} - n_{\text{Pb},i} E_{\text{PbI}_2}, \quad (2)$$

where index  $i$  indicates the configuration at hand, and  $n_{\text{Cs},i}$  and  $n_{\text{Pb},i}$  are the number of Cs and Pb- atoms in a unit cell, respectively. The results are shown in Table 1. Whereas the energies of slabs with  $\text{CsI}$ -terminations follow a similar trend to the bulk material, those of  $\text{PbI}_2$ -terminated slabs do not. This could be a result

of the presence of a larger number of open bonds at the boundaries of  $\text{PbI}_2$ -terminated slabs, compared to  $\text{CsI}$ -terminated slabs. The destabilizing effect of these open bonds may be enhanced by the increasing irregularity toward the  $\gamma$ -structure. Furthermore, the  $\beta$ - and  $\gamma$ -phases of the  $\text{CsI}$ -terminated slabs are the only slab configurations that are stable w.r.t. their separate  $\text{PbI}_2$ - and  $\text{CsI}$ -components, meaning that all other slab configurations are unstable and are likely to disintegrate into separate  $\text{PbI}_2$  and  $\text{CsI}$  molecules.

A different source of instabilities is the surface interface of the  $\text{CsPbI}_3$ . The  $\text{PbI}_2$  and  $\text{CsI}$  surfaces are investigated for their inherent stability. Using MD simulations it is shown that the  $\text{PbI}_2$  interface is more unstable than the  $\text{CsI}$  interface. This is specifically prevalent in higher temperatures. In Fig. 2b the  $\text{PbI}_2$  surface is breaking apart at a temperature of 700 K. This is most likely due to missing bonds in this lead iodine surface. Which causes a high surface energy and is, therefore, a less favourable configuration.<sup>31</sup> In simulations with a temperature below 700 K, the surface did not degrade during the entire simulation of 1.25 ns, this might mean that the surface instability, in this case, is linked to the temperature, however, this does not give any conclusion on long term stability.

### 3.2 Lattice parameters

A comprehensive analysis of the structural properties is necessary to explain possible differences in optical and electronic properties of the various phases.<sup>31</sup> We look at the  $\text{Pb-Pb}$  bond length and the  $\text{I-I-I}$  angle as depicted in Fig. 4. The bond lengths and angles of the material calculated using MD and DFT are given in Table 2. We see that the experimental data is in good agreement with the DFT calculations for the bulk, hence the relaxation of the material is adequate. The bond lengths in the slab are different from the bond lengths in the bulk for all phases, where the lengths all decrease in the slab. The atoms tend to move closer together, which should be the case. In bulk, the Coulomb forces between the layers are all equal, since the layers are equally separated. However, in the periodic slabs, the layers are separated more, so the atoms in one slab will have a smaller counteracting Coulomb force, and the atoms move closer to each other in the slab. This effect is more pronounced in the top or bottom layer, since there is no layer above or below respectively there, having an even smaller counteracting Coulomb force. We see these effects occur in all phases.

Using MD relaxation approximately the same values for the bulk structures are obtained. In the slab structures, a difference is observed. Whereas the  $\text{Pb-Pb}$

Table 2: Structural and electronic properties of  $\text{CsPbI}_3$  found using DFT and MD calculations compared to experimental data. Experimental bond lengths and angles from Maronnier<sup>27</sup> and experimental band gaps from Filip,<sup>28</sup> Wang,<sup>29</sup> and Straus.<sup>30</sup>

Phase		Length ( $\text{\AA}$ )		Angle ( $^\circ$ )		Bandgap (eV)	
		Bulk	Slab	Bulk	Slab	Bulk	Slab
Cubic	DFT	6.37	Outer 6.32	90.00	Outer 90.91	1.46	1.37
			Inner 6.34		Inner 90.98		
	MD	6.29	Outer 6.38	90.00	Outer 85.44		
			Inner 6.33		Inner 88.60		
	Exp.	6.30		90.00		1.68	
Tetragonal	DFT	6.46	Outer 6.34	90.05	Outer 90.14	1.59	1.42
			Inner 6.39		Inner 90.98		
	MD	6.40	Outer 6.49	90.16	Outer 84.61		
			Inner 6.42		Inner 87.34		
	Exp.	6.30		89.87		1.68	
Orthorhombic	DFT	6.33	Outer 6.23	73.08	Outer 71.87	1.79	1.72
			Inner 6.28		Inner 71.24		
	MD	6.24	Outer 6.42	71.85	Outer 73.20		
			Inner 6.30		Inner 72.07		
	Exp.	6.25		74.43		1.63	



distance decreases in slabs using DFT, this distance increases when MD relaxation is used. The discrepancy is likely due to a difference in constraints. Slab simulations in DFT neglected the cell shape and volume as degrees of freedom, whereas MD did not have this constraint. Also, the MD simulations use a reactive force field, which is based on DFT calculations. This force field is only an approximation of the actual forces that play a role in the system.

### 3.3 Electronic properties

To analyze the electronic character, band structures are calculated for each phase. The band structure for bulk  $\alpha$ -CsPbI<sub>3</sub> is depicted in Figure 5. Here, the minimum of the conduction band and the maximum of the valence band are both located at the high symmetry R point, which means that this phase has a direct band gap. Although the band gap is located at other symmetry points for slabs and other bulk structures, the band gaps are still direct for all phases, which is desirable for semiconductors. The values of the band gaps are reported in Table 2. The calculated band gaps agree reasonably well with the experimental values, but the found structural parameters are relatively more accurate. This was to be expected since standard DFT calculations do not predict the band gaps very accurately.<sup>32</sup>

The band gap becomes larger for a smaller Pb–Pb bond length for  $\alpha$ - and  $\beta$ -CsPbI<sub>3</sub>, both in bulk and in slab, but not for  $\gamma$ -CsPbI<sub>3</sub>. This behaviour of  $\alpha$ - and  $\beta$ -CsPbI<sub>3</sub> was to be expected since the binding forces would increase and the valence electrons would be more bound, hence increasing the band gap. The orthorhombic struc-

ture behaves differently, however, possibly as a result of a higher atom density in the structure. Still, the band gap is also lower in the slab than the bulk for the orthorhombic structure, which does correspond to the expected behaviour. To explain the electronic behaviour in more detail, more accurate band structure calculations should be done using the DFT-1/2 method,<sup>33</sup> for instance.

## 4 Conclusion

We have investigated stability, structural properties and electronic properties of different phases of CsPbI<sub>3</sub> in bulk and slab configurations. DFT calculations show that the  $\gamma$ -CsPbI<sub>3</sub> is the most stable perovskite phase in bulk and slab. The CsI terminated slabs are more stable compared to PbI<sub>2</sub> terminated slabs, partly because PbI<sub>2</sub> clusters form in the latter, destabilizing the material. The formation energies of CsI terminated slabs are lower as well.

Furthermore, the found lattice parameters in the bulk material are in good agreement with experimental results, indicating that DFT and MD are both appropriate methods to calculate structural properties. However, the values for the bond lengths from the DFT and MD simulations do not match. The values decrease for slabs when compared to the bulk for DFT, but increase in MD calculations.

Lastly, DFT was used for band structure calculations. The band gap increases for structures where the interatomic distance is smaller, except for the  $\gamma$  phase. The band gap does correspond reasonably well to experimental values, but more accurate calculations should be done for quantitative results and to explain why the band gap increases for  $\gamma$  phase.

## 5 Conflicts of interest

The authors declare no conflict of interest.

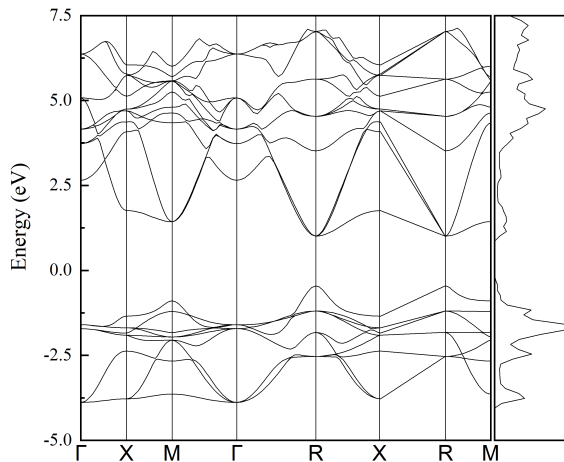


Figure 5: Calculated band structure and density of states of cubic CsPbI<sub>3</sub>.

## References

- (1) IEA Global Energy Review 2021.
- (2) Wang, D.; Wright, M.; Elumalai, N. K.; Uddin, A. *Solar Energy Materials and Solar Cells* **2016**, *147*, 255–275.
- (3) Eperon, G. E.; Paternò, G. M.; Sutton, R. J.; Zampetti, A.; Haghighirad, A. A.; Cacialli, F.; Snaith, H. J. *Journal of Materials Chemistry A* **2015**, *3*, 19688–19695.
- (4) Li, B.; Zhang, Y.; Fu, L.; Yu, T.; Zhou, S.; Zhang, L.; Yin, L. *Nature communications* **2018**, *9*, 1–8.
- (5) Zhang, T.; Dar, M. I.; Li, G.; Xu, F.; Guo, N.; Grätzel, M.; Zhao, Y. *Science advances* **2017**, *3*.
- (6) Zhang, T.; Li, H.; Ban, H.; Sun, Q.; Shen, Y.; Wang, M. *Journal of materials chemistry A* **2020**, *8*, 4118–4124.
- (7) Yao, Z.; Zhao, W.; Liu, S. F. *Journal of Materials Chemistry A* **2021**, *9*, 11124–11144.
- (8) Shockley, W.; Queisser, H. J. *Journal of Applied Physics* **1961**, *32*, 510–519.
- (9) Xue, J.; Wang, R.; Yang, Y. *Nature Reviews Materials* **2020**, *5*, 809–827.
- (10) Rüger, R.; Franchini, M.; Trnka, T.; Yakovlev, A.; van Lenthe, E.; Philipsen, P.; van Vuren, T.; Klumpers, B.; Soini, T. AMS, version 2022.1, SCM.
- (11) Van Duin, A. C. T.; Dasgupta, S.; Lorant, F.; Goddard, W. A. *The Journal of Physical Chemistry A* **2001**, *105*, 9396–9409.
- (12) Chenoweth, K.; van Duin, A. C. T.; Goddard, W. A. *The Journal of Physical Chemistry A* **2008**, *112*, PMID: 18197648, 1040–1053.
- (13) Van Duin, A.; Goddard, W.; Islam, M.; van Schoot, H.; Trnka, T.; Yakovlev, A. ReaxFF, version 2022.1, SCM.
- (14) Pols, M.; Vicent-Luna, J. M.; Filot, I.; van Duin, A. C. T.; Tao, S. *The Journal of Physical Chemistry Letters* **2021**, *12*, 5519–5525.
- (15) Jain, A.; Ong, S. P.; Hautier, G.; Chen, W.; Richards, W. D.; Dacek, S.; Cholia, S.; Gunter, D.; Skinner, D.; Ceder, G.; Persson, K. A. *APL Materials* **2013**, *1*, 011002.
- (16) Berendsen, H. J. C.; Postma, J. P. M.; van Gunsteren, W. F.; DiNola, A.; Haak, J. R. *The Journal of Chemical Physics* **1984**, *81*, 3684–3690.
- (17) Momma, K.; Izumi, F. *Journal of Applied Crystallography* **2011**, *44*, 1272–1276.
- (18) Kresse, G.; Furthmüller, J. *Phys. Rev. B* **1996**, *54*, 11169–11186.
- (19) Kresse, G.; Furthmüller, J. *Computational Materials Science* **1996**, *6*, 15–50.
- (20) Kresse, G.; Hafner, J. *Phys. Rev. B* **1994**, *49*, 14251–14269.
- (21) Kresse, G.; Hafner, J. *Phys. Rev. B* **1993**, *47*, 558–561.
- (22) Perdew, J. P.; Burke, K.; Ernzerhof, M. *Phys. Rev. Lett.* **1996**, *77*, 3865–3868.
- (23) Perdew, J. P.; Burke, K.; Ernzerhof, M. *Phys. Rev. Lett.* **1997**, *78*, 1396–1396.
- (24) Sutton, R. J.; Filip, M. R.; Haghighirad, A. A.; Sakai, N.; Wenger, B.; Giustino, F.; Snaith, H. J. *ACS Energy Letters* **2018**, *3*, 1787–1794.
- (25) Wang, X.; Wang, Y.; Chen, Y.; Liu, X.; Zhao, Y. *Advanced Materials* **2021**, *33*, 2103688.
- (26) Li, Y.; Zhang, C.; Zhang, X.; Huang, D.; Shen, Q.; Cheng, Y.; Huang, W. *Applied Physics Letters* **2017**, *111*.
- (27) Marronnier, A.; Roma, G.; Boyer-Richard, S.; Pedesseau, L.; Jancu, J.-M.; Bonnassieux, Y.; Katan, C.; Stoumpos, C. C.; Kanatzidis, M. G.; Even, J. *ACS nano* **2018**, *12*, 3477–3486.
- (28) Filip, M. R.; Eperon, G. E.; Snaith, H. J.; Giustino, F. *Nature communications* **2014**, *5*, 1–9.
- (29) Wang, Y.; Dar, M. I.; Ono, L. K.; Zhang, T.; Kan, M.; Li, Y.; Zhang, L.; Wang, X.; Yang, Y.; Gao, X.; Qi, Y.; Grätzel, M.; Zhao, Y. *Science* **2019**, *365*, 591–595.
- (30) Straus, D. B.; Guo, S.; Cava, R. J. *Journal of the American Chemical Society* **2019**, *141*, 11435–11439.
- (31) Liu, D.; Shao, Z.; Li, C.; Pang, S.; Yan, Y.; Cui, G. *Small Structures* **2021**, *2*, 2000089.
- (32) Brivio, F.; Butler, K. T.; Walsh, A.; Van Schilfgaarde, M. *Physical Review B* **2014**, *89*, 155204.
- (33) Tao, S. X.; Cao, X.; Bobbert, P. A. *Scientific reports* **2017**, *7*, 1–9.